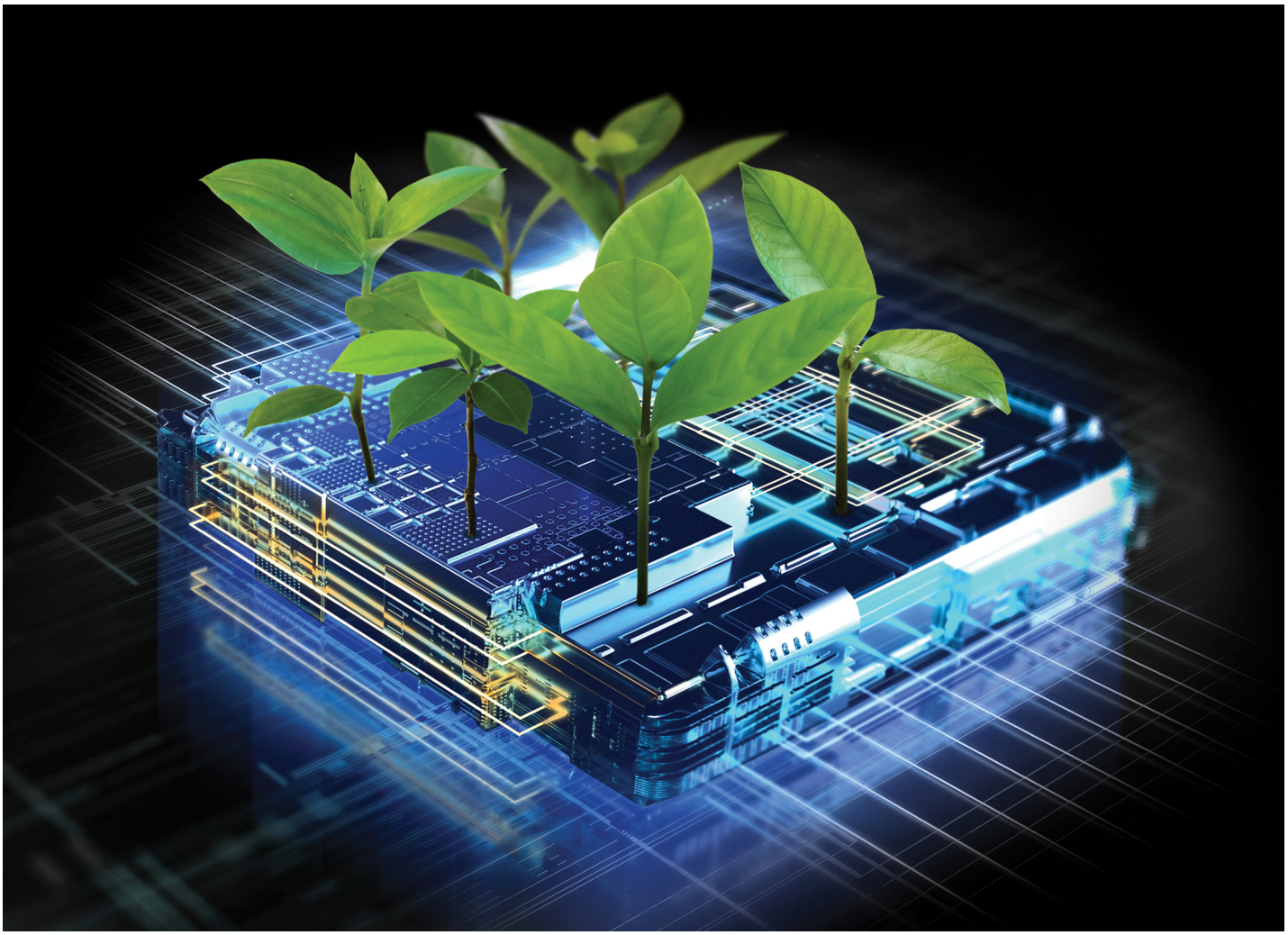

Showcasing research from the group of Dr Oleg Poluektov at Argonne National Laboratory, USA

Light-induced electron spin qubit coherences in the purple bacteria reaction center protein

This study utilizes high-frequency electron paramagnetic resonance spectroscopy to investigate spin coherence in purple bacteria reaction center proteins. It examines the role of local molecular environments and isotopic substitutions on spin-correlated radical pairs formed during light-induced electron transfer. The findings highlight how protein microenvironments and methyl group dynamics influence spin decoherence. These insights advance strategies for optimizing coherence times in quantum information science and sensing applications.

As featured in:

See Oleg G. Poluektov *et al.*, *Phys. Chem. Chem. Phys.*, 2025, **27**, 19651.

ROYAL SOCIETY OF CHEMISTRY

rsc.li/pccp

Registered charity number: 207890

PCCP Owner Societies

PCCP

PAPER

View Article Online
View Journal | View Issue

Cite this: *Phys. Chem. Chem. Phys.*, 2025, **27**, 19651

Light-induced electron spin qubit coherences in the purple bacteria reaction center protein†

Jasleen K. Bindra, Jens Niklas, Yeonjun Jeong, Ahren W. Jasper, Lisa M. Utschig and Oleg G. Poluektov *

Photosynthetic reaction center proteins (RCs) provide ideal model systems for studying quantum entanglement between multiple spins, a quantum mechanical phenomenon wherein the properties of the entangled particles become inherently correlated. Following light-generated sequential electron transfer, RCs generate spin-correlated radical pairs (SCRPs), also referred to as entangled spin qubit (radical) pairs (SQPs). Understanding and controlling coherence mechanisms in SCRP/SQPs is important for realizing practical uses of electron spin qubits in quantum sensing applications. The bacterial RC (bRC) provides an experimental system for exploring quantum effects in the SCRP P_{865}^{+} Q_A^{-}, where P_{865}, a special pair of bacteriochlorophylls, is the primary donor, and Q_A is the primary quinone acceptor. In this study, we focus on understanding how local molecular environments and isotopic substitution, particularly deuteration, influence spin coherence times (T_M). Using high-frequency electron paramagnetic resonance (EPR) spectroscopy, we observed that the local environment surrounding P_{865} and Q_A plays a significant role in determining T_M. Our findings show that while deuteration led to a modest increase in T_M, particularly at low temperatures, but the effect was substantially smaller than predicted by classical nuclear spin diffusion alone. This result is in contrast to our previous study of the photosystem I (PSI) RC, where no increase in T_M was observed upon deuteration. Theoretical modeling identified several methyl groups at key distances from the spin centers of both bRC and PSI, and methyl group tunneling at low temperatures has been previously suggested as a mechanism for enhanced spin decoherence. Additionally, our study revealed a strong dependence of spin coherence on the orientation of the external magnetic field, highlighting the influence of the protein microenvironment on spin dynamics. These results offer new insights for optimizing coherence times in quantum system design for quantum information science and sensing applications.

Received 15th October 2024,
Accepted 6th January 2025

DOI: 10.1039/d4cp03971h

rsc.li/pccp

Introduction

In quantum information science, the coherence time—the duration during which a quantum system retains its quantum state—is a critical parameter. Extended coherence times are essential for the practical implementation of quantum computing and communication technologies, ensuring the reliability and effectiveness of quantum operations. However, maintaining coherent states for sufficiently long durations remains a significant challenge in the field.[1–7]

Electron spins are excellent candidates for quantum bits (qubits) due to their two spin states, which form an ideal two-level quantum system capable of superposition. Coupling electron spins through spin–spin exchange (J) and dipolar (D) interactions facilitate quantum entanglement and enable the implementation of two-qubit gates, essential for quantum operation. Despite their potential, generating well-defined initial quantum states and maintaining their coherence for extended periods is difficult. Achieving high spin polarization typically necessitates extremely low temperatures and strong magnetic fields, complicating practical applications.[4,6,7]

Spin-correlated radical pairs (SCRPs) present a promising solution to these challenges. Photogenerated SCRPs can function as qubits and spin qubit pairs. These pairs can exist in singlet and triplet spin states, forming a quantum superposition state. Their synthetic accessibility, well-defined structures, ability to be prepared in pure, entangled spin states, and optical addressability make SCRPs a promising avenue for quantum information science.[8,9]

The unique sensitivity of SCRP spin dynamics to external magnetic fields can be attractive for applications such as

Chemical Sciences and Engineering Division, Argonne National Laboratory, 9700 South Cass Avenue, Lemont, Illinois 60439, USA. E-mail: oleg@anl.gov

† Electronic supplementary information (ESI) available: ESI including temperature dependence of field swept ESE and ESEEM recorded at D band (130 GHz) for all samples and theoretical calculations of NSD coherence times T_M for the quinone electron spin for protonated and deuterated Zn bRC. See DOI: https://doi.org/10.1039/d4cp03971h

resolution-enhanced imaging, magnetometers, and magnetic switches.[10–23] The Wasielewski group pioneered usage of SCRP as qubits in quantum information science, successfully demonstrating a gate operation and quantum teleportation.[24–26] Another notable application of SCRPs is in the magnetic compass sense of migratory songbirds. These birds utilize the Earth's magnetic field (approximately 50 μT) for navigation, with cryptochrome flavoproteins in their photoreceptor cells acting as primary sensors. Light-induced electron transfer reactions within these proteins generate a magnetically sensitive flavin–tryptophan radical pair, forming a signaling state that encodes the magnetic field direction based on quantum yield of charge recombination reaction.[27,28]

Photosynthetic reaction centers (RCs) provide natural models for studying SCRPs.[10–16,20,22,29–31] In these systems, ultrafast electron transfer (ET) processes lead to stabilized charge separation, which is crucial for the initial photon-to-charge energy transduction in photosynthesis. The structural organization of these RCs, revealed by X-ray crystallography, shows two branches of protein embedded cofactors arranged in pseudo twofold symmetry, each containing primary electron donors, intermediate chlorophylls, and quinones that facilitate ET. RCs are classified as either Type I or Type II based on their terminal electron acceptor cofactor (Fig. 1). ET in Type II RCs is unidirectional occurring through only one branch of cofactors whereas ET in Type I RCs is bidirectional and can proceed through both branches of cofactors.[13–16,32,33]

In the Type II purple non-sulfur bacterial RC (bRC), the primary electron donor, P_{865}, is a dimer of bacteriochlorophyll molecules. Upon photoexcitation of P_{865}, an electron is transferred through the bacteriopheophytin (I_A) to the primary quinone acceptor Q_A, stabilizing a transient charge-separated state $P_{865}^{+}Q_A^{-}$.[34–38] In *Rhodobacter* (now called *Cereibactor*) *sphaeroides*, the electron is transferred within 200 ps from the excited singlet state of P_{865} to Q_A. The ET sequence continues from Q_A to the secondary quinone acceptor Q_B. Following a two-electron, two-proton reduction, Q_BH_2 is released from the protein, delivering reducing equivalents to the plastoquinone pool, completing the cycle. The bRC contains a non-heme Fe^{2+} located between Q_A and Q_B. The EPR active Fe^{2+} ion is strongly coupled with nearby reduced quinones which considerably enhance their spin relaxation beyond the time resolution of pulsed EPR spectrometers. To overcome this effect, the Fe^{2+} can be replaced with the non-paramagnetic Zn^{2+}. Multiple studies have shown that this replacement does not influence the functionality of the bRC.[30,39]

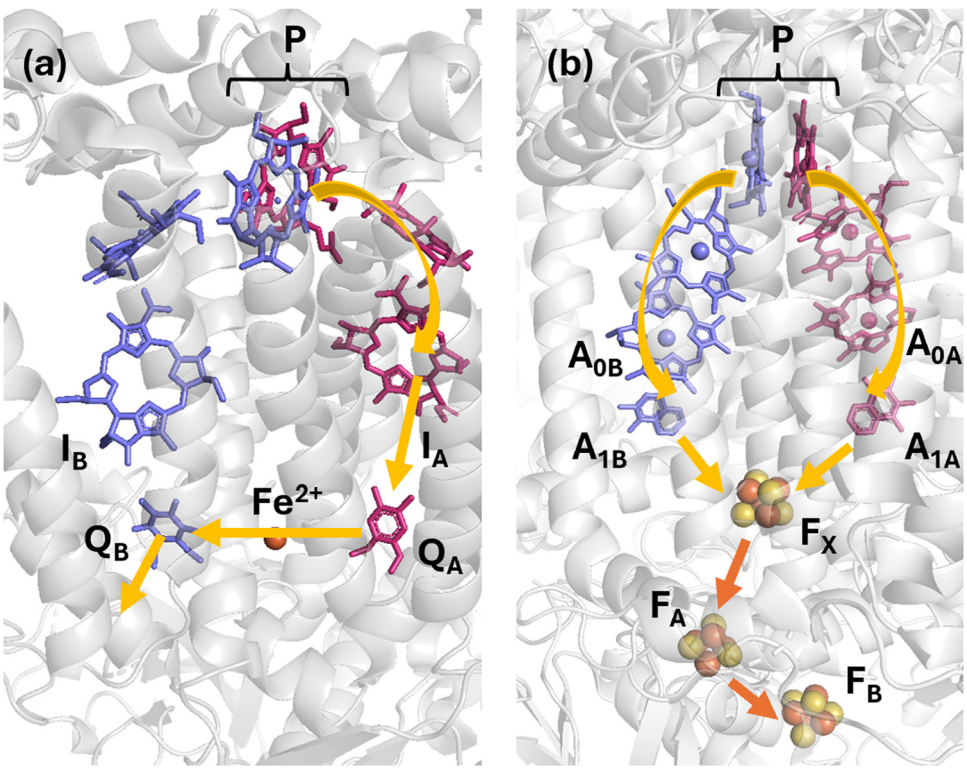

Fig. 1 Schematic structure and ET pathways in photosynthetic RCs of Type II (a) and Type I (b). The donor and acceptor cofactors in Type II and Type I photosynthetic RCs are arranged in two symmetric branches, A (red) and B (blue). (a) Type II bacterial RC from *Rhodobactor sphaeroides*. The primary donor P is a pair of bacteriochlorophyll molecules. The intermediate acceptors $I_{A/B}$ are bacteriopheophytins, and the terminal acceptors $Q_{A/B}$ are ubiquinone molecules positioned around a nonheme Fe ion. The unidirectional ET pathway is indicated by arrows. After a two-electron, two-proton reduction Q_BH_2 is released from the RC, transporting electrons and protons to other redox components in the bacterium.[32] (b) Type I photosystem I, PSI, RC from cyanobacterium. Following photoexcitation, the primary donor P becomes oxidized, transferring its electron to one of two identical chains of donor/acceptor molecules: a chlorophyll A_0, phylloquinone A_1, and three [4Fe–4S] clusters, F_X, F_A, and F_B. Photoinduced ET in PSI is bidirectional, proceeding through both the A and B branches of cofactors as indicated by arrows.[13,15–17]

The early ET steps are ultrafast and the charge-separated P_{865}^{+} Q_A^{-} pair is a SCRP. SCRPs are renowned for their extreme sensitivity to protein structure and dynamics but suffer in terms of decoherence because of strong interactions with their microenvironment. In our recent study of the Type I Photosystem I (PSI) RC, it was suggested that the low-temperature dynamics of methyl (and potentially amino) groups could govern decoherence in photosynthetic proteins.[40,41] This explanation aligns with several experimental and theoretical studies on model systems, where methyl group rotation, libration, and tunneling have been shown to substantially enhance decoherence at low temperatures.[42–48] Similar factors are likely to limit the coherence time in other photosynthetic reaction center proteins. Thus, the protein local structure, with its specific arrangements and dynamics of molecular groups, could directly impact decoherence processes by altering the local heterogeneous microenvironments around the electron spins, affecting how quickly and efficiently these spins lose their quantum coherence. The relationship between spin decoherence and protein structure makes a theoretical investigation for spin decoherence of SCRPs a highly desirable research objective.

Here, we report an investigation of light-induced electron spin coherences in the bRC protein. The goal of this study is to explore how the local environment of these proteins influences spin decoherence times, a critical parameter for quantum information science. The study examines the effects of partial and full deuteration on spin coherence, emphasizing the role of the local molecular dynamics, particularly the methyl group, in modulating electron spin decoherence. By utilizing high-frequency electron paramagnetic resonance (EPR) spectroscopy and advanced computational models, the research seeks to elucidate the mechanisms driving spin decoherence in these photosynthetic systems.

Experimental

Sample preparation

Deuterated RCs were isolated from the whole cells of *R. sphaeroides* R-26 (now *Cereibacter sphaeroides*), which were grown in heavy water (99.7% D_2O) on deuterated substrates. Protonated RCs were isolated from the whole cells of *R. sphaeroides* R-26 (now *Cereibacter sphaeroides)* grown in H_2O on protonated substrates. All EPR measurements were done on Zn-substituted bRCs (Zn bRCs) where Fe was removed and substituted by Zn. The Fe-removal/Zn-substitution was done on isolated bRCs as previously described in H_2O buffered solutions.[39,49] For incorporation of deuterated Q_A in protonated Zn-substituted bRCs, deuterated ubiquinone-10 was used in place of protonated ubiquinone-10 in the protocol.[50]

EPR spectroscopy

EPR measurements were performed on a pulsed/continuous wave high frequency D-band (130 GHz/4.6 T) EPR spectrometer with a single mode TE_{011} cylindrical cavity.[51,52] Pulsed EPR spectra of stable radical species were recorded by monitoring the electron spin echo (ESE) intensity from a two-microwave pulse sequence as a function of magnetic field. Pulsed TR-EPR spectra of the SCRPs were recorded in a similar way by initial photoexcitation of the protein by a short (<10 ns) laser pulse followed by a fixed delay after flash (DAF) time before the microwave pulses (laser flash-t_{DAF}-$\pi/2$-τ-π-τ-echo). The duration of the $\pi/2$ microwave pulse was 40–60 ns. The decoherence was measured by recording ESE as a function of separation between microwave pulses, as well as monitoring Rabi oscillation decay. Light excitation of the sample was achieved with an optical parametric oscillator (OPO; basiScan, GWU Lasertechnik, Germany) pumped by a Nd: YAG laser (Quanta-Ray INDI, Spectra Physics), the output of which was coupled to an optical fiber. The optical fiber allows delivery of up to 2 mJ per pulse to the sample. The excitation wavelength was 550 nm.

The samples were loaded into quartz tubes (inner diameter 0.5 mm per outer diameter 0.6 mm), dark-adapted, and placed in the pre-cooled microwave cavity. The cavity was mounted in an Oxford flow cryostat, and temperature was controlled by an Oxford temperature control system (ITC503).

Results and discussion

Experimental

In the photosynthetic bRC, an electron is transferred from the primary donor P_{865} to the acceptor Q_A after light excitation on hundreds of picoseconds timescale. At low temperatures, the electron transfer to Q_B is blocked. The spin correlated radical pair P_{865}^{+} Q_A^{-} is formed in the singlet state which leads to the spin-polarized EPR spectra. Time resolved EPR spectroscopy has been extensively used in the study of the radical pair P_{865}^{+} Q_A^{-}. The spin-polarized spectrum of this state provides structural information about the spin system, the interaction of the radicals with the protein environment as well as kinetic information about the sequential charge separation process.[12,20,29,30,53,54]

Fig. 2 shows the high-frequency D-band field-swept pulsed electron spin echo (ESE) spectra of deuterated *Cereibacter sphaeroides* obtained by recording echo intensity as a function of magnetic field. D-Band field-swept ESE spectra of the bRC sample recorded upon laser excitation with 700 ns DAF time (see Fig. 3a) in dark, before light excitation (black, ''dark'') and in a time resolved mode (green, ''light'') are shown in Fig. 2a. The dark-adapted bRC shows a ''dark'' (Fig. 2a, black) signal within the range of 4.634–4.637 T. In the ''light'' spectrum (Fig. 2a, green), strong additional emission/absorption signals at lower magnetic fields are observed. This is the spin-polarized signal of the quinone acceptor, Q_A^{-}, as part of the P_{865}^{+} Q_A^{-} SCRP. The difference spectrum (''light minus dark'', Fig. 2a, red) is a ''pure'' spectrum of the SCRP P_{865}^{+} Q_A^{-} in Zn bRC. The low-field part of the spectra represents the signal from the reduced quinone acceptor Q_A^{-}, while the high-field part of the spectra is dominated by signals from the primary donor P_{865}^{+}. The g_x and g_y components of the rhombic g-tensor of P_{865}^{+} in

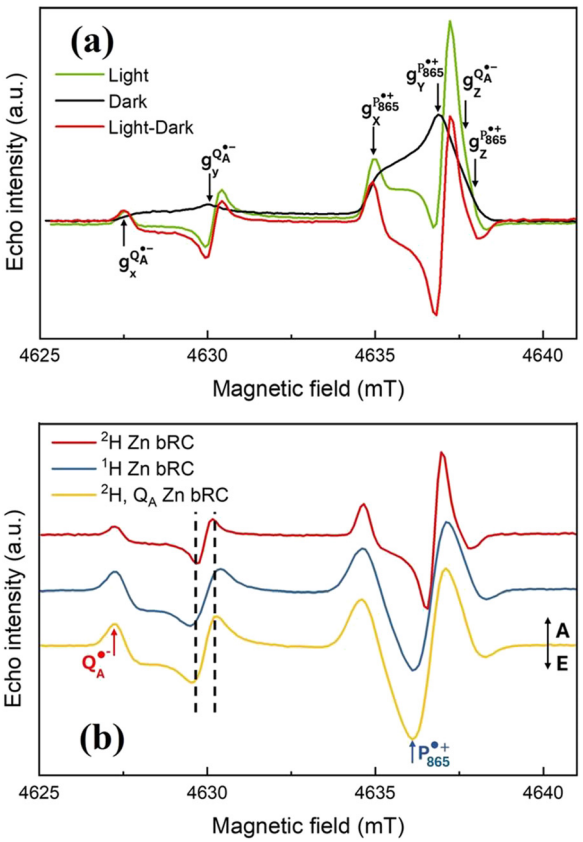

Fig. 2 (a) Typical D-band field-swept pulsed ESE spectra of a deuterated bacterial reaction center sample recorded in the "dark" (black), "light" (green), and the "light" minus "dark" difference (red). The SCRP spectrum (red) is consistent with our previously published spectra.[20] Arrows show the canonical positions of the g-tensors (g_x, g_y and g_z) for P_{865}^+ and Q_A^-. (b) SCRP spectra from Zn bRCs with different biochemical treatments. Spectra were recorded as the difference "light" minus "dark" with a DAF time 700 ns. Arrows indicate the magnetic field positions where the two pulse ESE measurements were recorded. Note that the g_x and g_y regions of the partially deuterated sample (yellow) are narrower than those of the protonated sample (blue). The dashed lines in the figure are guide for the eye.

the range of 4.627 to 4.630 T are clearly resolved and well-separated from dark background signals. However, the g_z component of Q_A^-, corresponding to a magnetic field of 4.638 T, remains obscured due to significant overlap with the intense P_{865}^+ signal in this field range. These spectra are in good agreement with previously published high field/frequency EPR spectra, confirming the functionality of these complexes.[20,29,30,55,56]

Note that the use of high magnetic field/frequency improves both g-tensor resolution and absolute sensitivity compared to conventional X-band EPR spectroscopy. High g-tensor resolution enables the separation of signals from different spin centers with similar g-factors and the resolution of weakly anisotropic g-tensors.[20,52,55,57] The enhanced absolute sensitivity at high field/frequency is particularly advantageous in many biochemical and biophysical studies where only limited amounts of material are available. Further, deuteration of the sample reduces the inhomogeneous linewidth and increases the resolution of the spectra.[54,58] As seen in Fig. 2b the deuteration of only Q_A affects only the low field side of the spectra leaving the high field side of the spectra unaffected.

D-Band EPR spectra of Zn bRC differ significantly from X-band spectra. When recorded at the conventional X-band, EPR spectra of the donor P_{865}^+ and Q_A^- acceptor significantly overlap, whereas D-band enables the well-resolved and complete characterization of g-tensor anisotropy due to a 14 times higher g-tensor resolution.[20,52,55,57] Furthermore, at X-band pulsed EPR transitions of both spins in SCRPs are excited with a microwave pulse, resulting in complete excitation of the system. This leads to the observation of out-of-phase electron spin echo (ESE) modulation in addition to the conventional electron spin echo envelope modulation (ESEEM) which further complicates the analysis of the ESE decay.[31,59] At high frequency EPR, like D-band, the ESEEM effects are suppressed, and selective excitation of the spectra does not lead to the appearance of out-of-phase ESE, thus enabling more precise measurement of coherence decay, T_M.

Rabi oscillations are used to characterize qubit's coherence time by measuring the damping of their amplitudes.[1,2,60] In EPR spectroscopy, they're observed as the ESE intensity as a function of the nutation pulse length. Fig. 3 shows the microwave pulse sequence for detecting Rabi oscillations and the "light-dark" difference time traces, along with their temperature-dependent decay profiles. Measurements of P_{865}^+ and Q_A^- in protonated, deuterated and partially deuterated samples were fitted with a damped sine function given by: function $y_0 + A\exp\left[\frac{-x}{t_0}\right]\sin\frac{(2\pi(x-x_c))}{T}$, where y_0 is the offset, x is the length of the nutation pulse, x_c is the phase shift, T is the period, t_0 is decay constant and A is the amplitude. Temperature dependence indicates stable dephasing times (40–200 K), with minimal differences between protonated and deuterated samples. However, due to microwave B_1 field inhomogeneity in the EPR resonator, Rabi oscillation decay may underestimate spin coherence times and is unreliable for measuring phase memory time T_M. The two pulse ESE signal decay is considered as a direct measurement of the spin coherence (Fig. 4b). Two-pulse ESE decays were recorded for both P_{865}^+ and acceptor Q_A^-. Echo decay measurements in "dark" (green), upon laser excitation "light" (orange), their difference (blue) and fits with mono-exponential function (dash) are shown in Fig. 4b.

Typical two pulse ESE decay kinetics can be fit with a stretched exponential function : $E(2\tau) = \exp\left[-\left(\frac{2\tau}{T_M}\right)^c\right]$, where τ is the time between pulses, and the stretching parameter c. It has been shown that if nearby nuclei flop-flops (*i.e.* nuclear spin diffusion, NSD) is the main decoherence mechanism, then ESE decays can be fit by a stretched exponential function with c often found to be in the range of 2–2.5. In contrast, here ESE decay is observed to be exponential with stretching parameter c close to 1.[42,45,61–64] Fig. 4 and Fig. S4–S6 (ESI†) show decay kinetics as well as temperature dependence of decoherence

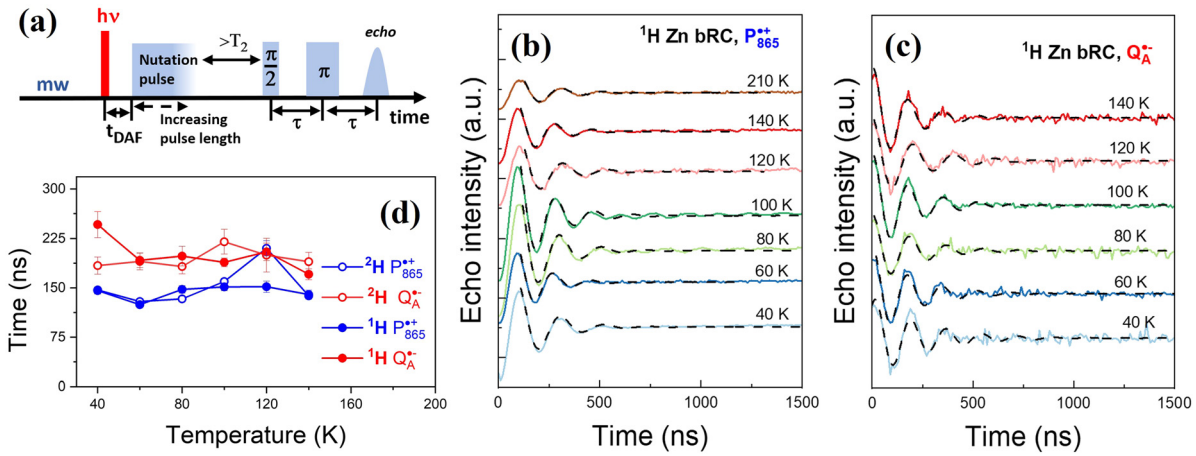

Fig. 3 Rabi oscillations recorded in protonated, deuterated, and partially deuterated Zn bRCs. (a) Microwave pulse sequence for recording Rabi oscillations. For light induced states, a <10 ns laser pulse at 550 nm was applied 700 ns (t_{DAF}) before the first π/2 microwave pulse. Data were recorded within an excitation bandwidth of *ca.* 10 MHz. (b) Rabi oscillations as a function of temperature recorded for "light–dark" state of P_{865}^{+}. (c) Rabi oscillations as a function of temperature recorded for "light–dark" state of Q_A^{-}. (d) Temperature dependence of the Rabi oscillation decay times, t_0, for "light–dark" states of P_{865}^{+} and Q_A^{-} in all Zn bRCs.

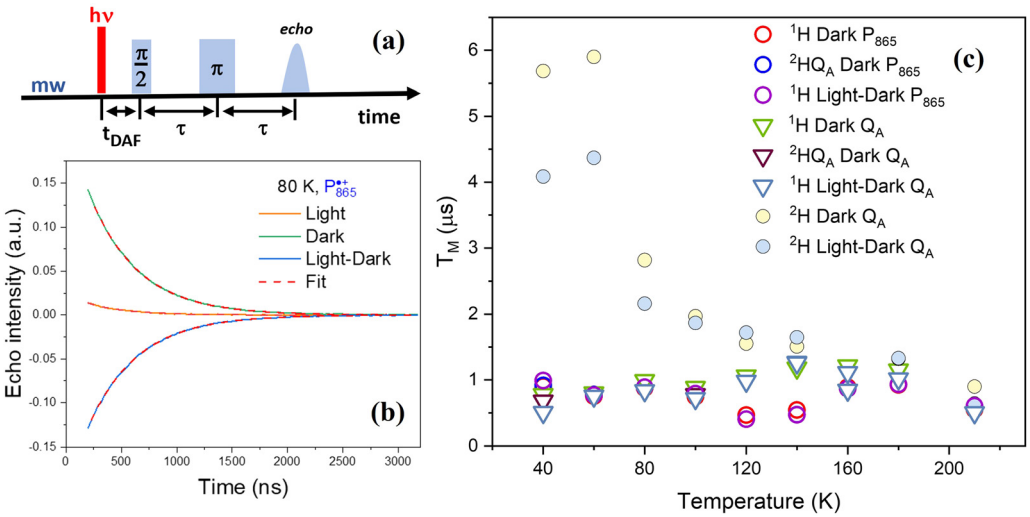

Fig. 4 Hahn-Echo decays recorded in protonated and deuterated PSI at D-band. (a) Microwave pulse sequence for recording Hahn echo decays. For light induced states the <10 ns laser pulse at 550 nm was applied 700 ns before the first π/2 microwave pulse. Data were recorded within an excitation bandwidth of *ca.* 10 MHz. (b) ESE decays of P_{865}^{+} in protonated Zn bRC at 120 K and fits with mono-exponential function. Time corresponds to time between first microwave pulse and echo (2τ). (c) Temperature dependence of T_M times for dark and difference ("light minus dark") states of both $P_{685}^{+}$and Q_A^{-} obtained for all samples upon fitting the ESE decays.

times for Zn bRC with different biochemical treatments. The experimental findings derived from our analysis of the data reveal intriguing insights into the dynamics of spin coherence in photosynthetic bRCs. Here, we summarize the key results and their implications for understanding the underlying mechanisms of spin decoherence.

First, there is considerable spread in T_M times observed in our experiment, especially at low temperatures. This phenomenon arises from additional modulations detected at low temperatures (Fig. 4c and Fig. S6, ESI†) that complicate the fitting of echo decays using standard exponential models making reliable data interpretation challenging and contributing considerably to the large errow of the experimental T_M times at low temparature. As previously mentioned, these modulations cannot be attributed to out-of-phase ESE or nuclear ESEEM, but rather to the tunneling dynamics of methyl groups in close proximity to radical centers within the protein environment.[40]

Interestingly, coherence times are found to be similar in the "dark" and "light–dark" (entangled spins states in SCRP) states for protonated bRC. Moreover, experiments involving partial deuteration, where only Q_A was deuterated, showed that the T_M

times measured on the protonated sample and the sample where only Q_A was deuterated were reproduced with high accuracy. This is an indication that the deuteration of Q_A does not extend the T_M times. This is reasonable as the nearest deuterons and protons are not very efficient contributors to spin diffusion.

At low temperatures where molecular motions are nearly frozen, a major mechanism for decoherence is nuclear spin diffusion (NSD), which is the loss of electron coherence due to spontaneous nuclear spin ''flip–flops'' in the nearest environment of the electron spin. When NSD is the dominant decay mechanism, full deuteration of the system could potentially lead to a substantial increase in coherence times, estimated at approximately 17 times longer compared to non-deuterated samples.[62] Surprisingly, in the fully deuterated Zn bRC we observed a more moderate increase, particularly notable at low temperatures where T_M times were 5–6 times higher. This contrasts with our previous measurements on PSI, where all three PSI samples from different species exhibited similar coherence times of 1–2 μs in the low-temperature range.[40] This is a clear indication that the standard NSD model cannot explain the complete set of experimental data.

Note that for fully deuterated samples at low temperatures, where spin coherences are around 5 μs, there is a clear difference in T_M times of Q_A^- between dark and light–dark states. For the SCRP the coherence time is 30% shorter. This effect in the protonated system is within the experimental error. Interestingly, in photosystem I, the coherence times were comparable in both the ''dark'' and ''light minus dark'' (entangled spins in SCRP) states. A similar effect is not observed for P_{865}^+, which we relate to the difference in the microenvironments (different number of nearby methyl groups) of P_{865}^+ and Q_A^-.

Both the bRC and PSI demonstrate the crucial role of the microenvironments in modulating spin coherence. In the bRC, coherence times are similar in both ''dark'' and ''light–dark'' states in fully protonated and protonated protein/deuterated quinone. Full deuteration can significantly increase coherence times at low temperatures, though the increase is more moderate in Zn bRCs, suggesting NSD alone cannot explain the experimental results. This leads us to the conclusion that, similar to PSI, the anisotropic protein structure and the dynamics of nearby residues, particularly methyl groups, play a significant role in regulating spin coherences. The tunneling dynamics of these groups at low temperatures enhance decoherence, suggesting that proteins can tune their microenvironment to regulate spin dynamics. This highlights the need for detailed theoretical and computational modeling to compare the decoherence mechanisms in Zn bRC with our previous results on PSI to fully understand these processes.

Theoretical

To calculate T_M, a detailed quantum treatment of the spin dynamics would in principle require tracking the density matrix and the time propagators for every electron and nuclear spin involved, rendering modeling the dynamics of systems with more than a few spins computationally challenging. The protein systems considered here consist of several thousands of relevant nuclear spins. To make the problem computationally tractable, the cluster-correlation expansion (CCE) approach was utilized,[65] which models the effects of NSD on the coherence of the center electron spin as a sum of the coherences resulting from bath nuclear spin clusters. PyCCE,[66] an open-source Python library developed by Onizhuk and Galli, was employed for this purpose. We ensured convergence of the key parameters in the CCE approach (the order of the CCE approximation, the maximum electron spin–bath nuclear spin interaction distance r_{bath}, and the maximum bath spin–bath spin interaction distance r_{dipole}), as shown in the Fig. S7 (ESI†).

The high-resolution crystal structure of the bRC for *Cereibacter sphaeroides* was taken from Koepke[67] *et al.* Open Babel[68] was used to add hydrogen atoms to the structure. No further modifications or optimizations of the structure were performed. The orientation of the external magnetic field was chosen to correspond to one of the three principal axes of the *g*-tensor of Q_A. The density matrix was propagated within the CCE approximation and, according to the Hahn-echo pulse sequence, the phase memory time T_M was calculated as the time at which the normalized electron spin echo intensity decayed to $1/e$.

The predicted phase memory times for the Q_A electron spin for the three magnetic field directions were found to be quite similar: $T_M^{bRC,x} = 5.61$ μs, $T_M^{bRC,y} = 5.81$ μs, and $T_M^{bRC,z} = 5.27$ μs. These values agree with those observed in glassy matrixes[42,61–63,69–72] and crystalline organic systems,[65,73,74] where NSD is the dominant spin decoherence mechanism, but much longer than the present experimental values discussed above of 1–2 μs. This discrepancy signifies that NSD is not the main decoherence mechanism for bRC and suggests enhanced decoherence from methyl group tunneling, a mechanism not present in the NSD calculations. Nonetheless, the NSD calculations allow us to characterize the local protein structure and to identify key chemical groups around the Q_A electron spin, as discussed next.

It is well known that clusters of protons enhance flip–flops and therefore enhance decoherence, and in the context of a protein environment (Fig. 5a) pairs and triples of protons most commonly exist within the methyl ($-CH_3$), methylene ($>CH_2$), and amino ($-NH_2$) functional groups and in water (H_2O). To identify key functional groups, we performed a series of tests where T_M was calculated with functional groups omitted one at a time. Within the present CCE model for NSD, removing one or more protons always results in a longer coherence time (although sometimes the increases can be negligible), and the resulting increase in T_M is denoted ΔT_M. Fig. 5b shows ΔT_M for functional groups near the electron spin on quinine plotted against the distance the contribution of these functional groups as measured by the increase of T_M in the absence of each group of protons. As previously observed in our study of PSI,[40,41] methyl groups are the dominant contributors. This can be explained by the fact that a methyl group possesses three proton pairs that can undergo fast flip–flops enhanced at low temperature by the tunneling dynamics. The distance range of 5–8 Å from the electron spin where there is the largest ΔT_M is

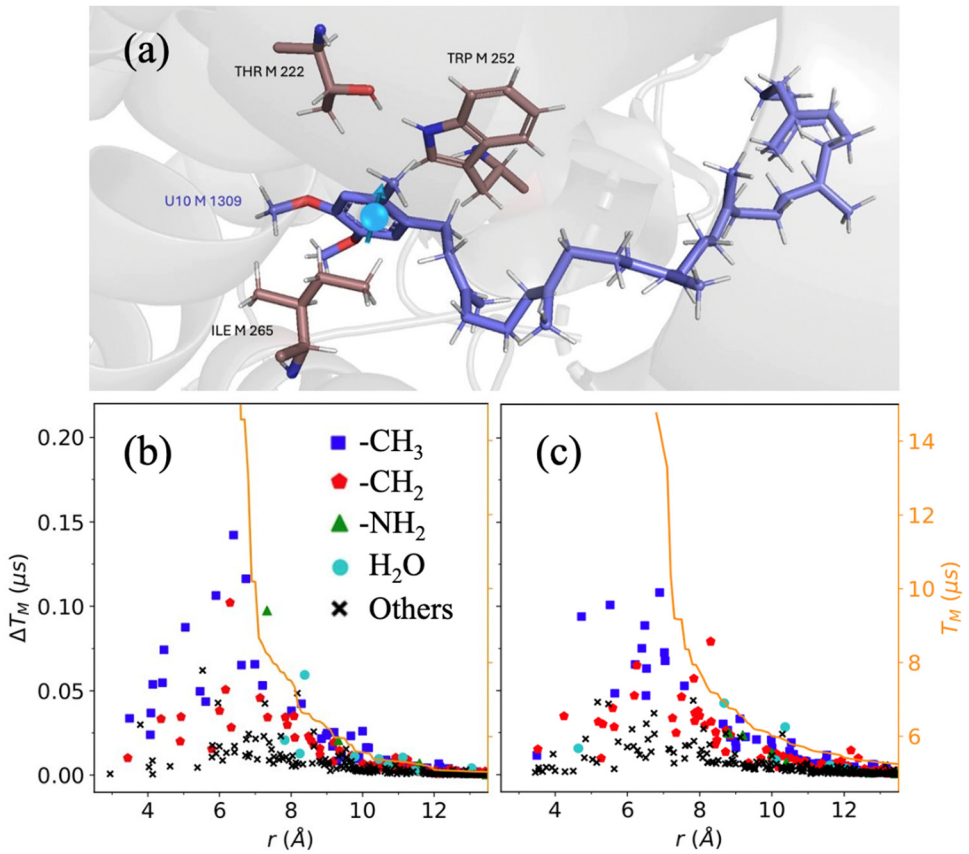

Fig. 5 (a) The local environment of the Q_A ubiquinone (U10) in the M chain of the photosynthetic reaction center of *Cereibacter sphaeroides*. The position of the electron spin is schematically described by a blue arrow. The atom colors are H (grey), C (purple for Q_A, and brown otherwise), N (blue), and O (red). (b) Functional group contribution to the NSD coherence time ΔT_M for the Q_A electron spin in bRC. The markers indicate $-CH_3$ (blue squares), $>CH_2$ (red pentagons), $-NH_2$ (green triangles), and H_2O (cyan circles). The protons that were not assigned to any of these functional groups are shown as black crosses (*x*). The calculated values of ΔT_M are plotted as a function the distance from the electron spin, *r*. The overlaid orange line is the coherence time calculated with all protons at distances greater than *r* removed. (c) The same information as in (b) but for the A_{1A}^- phylloquinone (PQN) electron spin in PSI.

also commonly typical of organic systems and was observed previously in PSI. The importance of this distance is confirmed by the orange line in Fig. 5, which shows the results of calculations where all protons at distances larger than *r* are removed.

In Fig. 5, the external magnetic field (B_0) was applied in the direction of the *x*-axis of the *g*-tensor of the Q_A site. We tested other field orientations, and although there is less than 10% difference in the calculated values of T_M for the three orientations, we found significant differences in the underlying details and in particular in which chemical groups contribute to the decoherence, as shown in Fig. S8 (ESI†). This highlights the fact that the relevant chemical groups are sensitive to the external magnetic field present in the decoherence process of the quinone electron spin.

The role of the external magnetic field orientation on the determination of the chemical moieties that participate in the decoherence of the electron spins is further emphasized by analyzing ΔT_M for artificial computations where entire residues and cofactors are removed (Fig. 6a). First, we compare these decoherence contributions of the residues and the cofactors for the Q_A^- site of bRC with the A_{1A}^- site of PSI (Fig. 6b). In both cases, the quinone (U10 for bRC and PQN for PSI) is the strongest single decoherence driver; both have methyl and methylene groups in abundance and in proximity to the electron spin. Both systems feature some similar residues of importance, *e.g.*, isoleucine (ILE) in bRC and leucine (LEU) in PSI, while threonine (THR) and asparagine (ASN) are uniquely present around bRC's Q_A and betacarotene (BCR) is only present in PSI's A_{1A}^- site. Next, we revisit magnetic field orientation for Q_A. The most important residues for the decoherence of Q_A^- depend on the field orientation, and no residue or cofactor is one of the three most important decoherers for all three field orientations other than the quinone itself, as indicated in Fig. 6c–e for Q_A.

The NSD calculations discussed so far do not include the enhanced decoherence mechanism due to methyl group tunneling. Model studies have found that methyl group tunneling substantially decreases coherence time of a nearby electron spin compared to when only the classical NSD mechanism is considered. To explore this additional mechanism, we increased the methyl proton–proton interaction artificially to mimic enhanced flip–flops due to tunneling. By increasing this

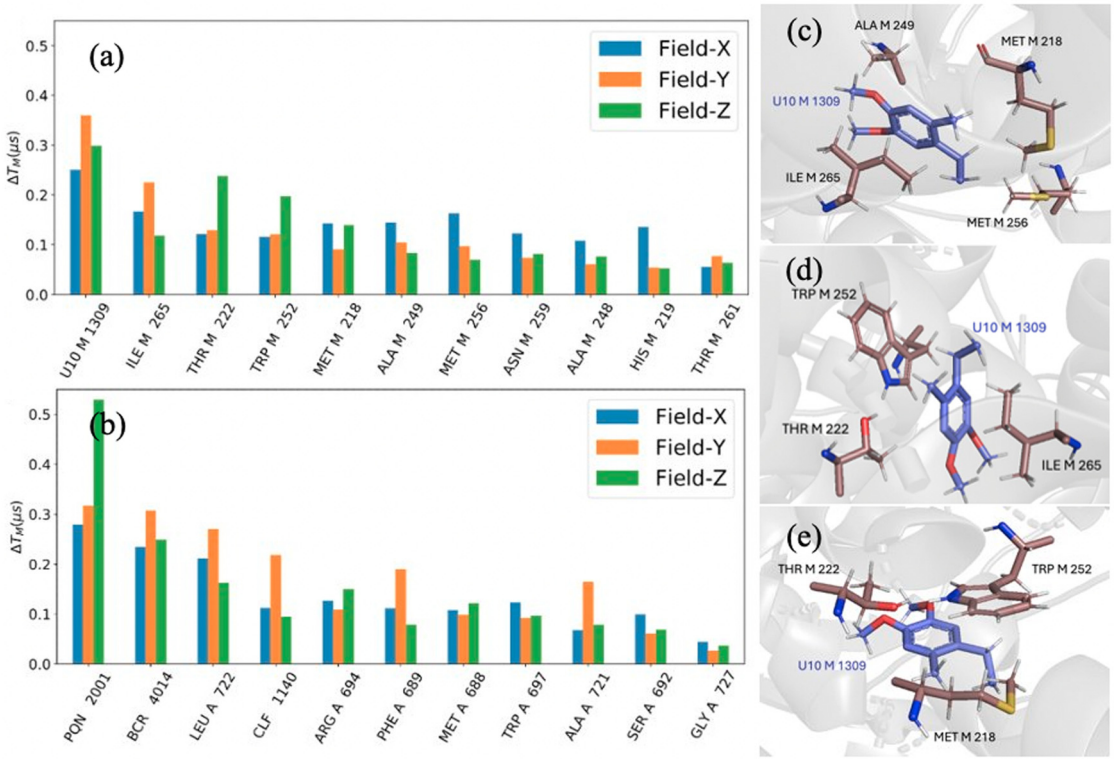

Fig. 6 The contributions of the residues and cofactors in the decoherence of the electron spin located at (a) Q_A^- (a ubiquinone) in the bRC (b) A_{1A}^- (a phylloquinone) of the PSI in *Synechococcus elongatus*, evaluated as the increase of T_M in the absence of each residue or cofactor, for the three magnetic field orientations corresponding the principal axes of the quinone *g*-tensor. The residues/cofactors are sorted in the descending order of the average of ΔT_M for the three field orientations. The residues and cofactors that are investigated were selected by choosing those who have at least one atom within 6 Å from the quinone's electron spin (assumed to be located at the center of the two oxygen atoms in the quinone ring). (c)–(e) The most dominant residue/cofactor contributors around Q_A for the field orientation *x*, *y*, and *z*, respectively.

parameter by a factor of 10, we found T_M = 1.5 μs, which is close to the experimentally observed value. For the fully-deuterated system, we found we had to increase the methyl deuteron–deuteron interaction by a factor of 50 to agree with the present experiment, giving T_M = 5.3 μs. Additional tests are summarized in Table S1 (ESI†).

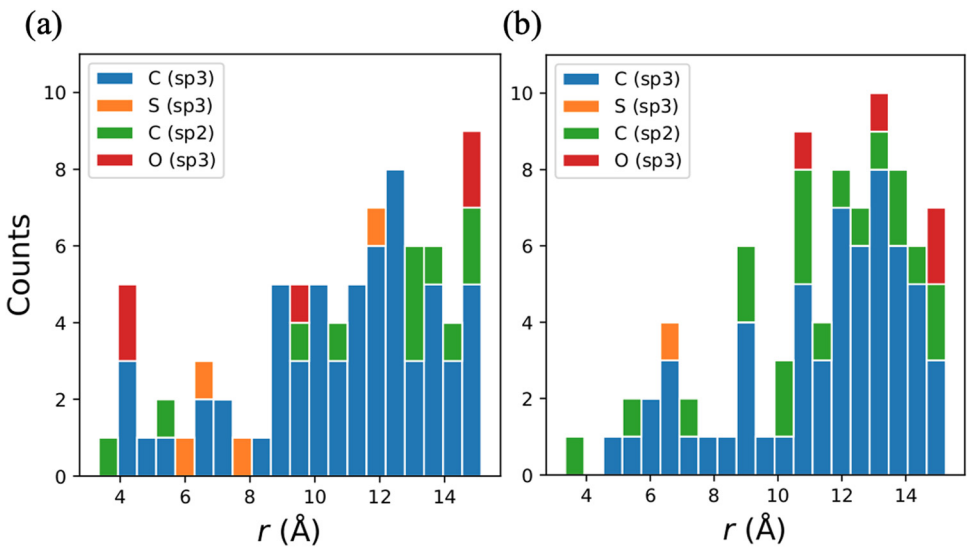

Fig. 7 The distribution of the distance between the methyl groups and the electron spin, *r*, near (a) Q_A in bRC and (b) A_{1A}^- in PSI. The average position of the three hydrons of the methyl groups and the average position of the two sp^2 oxygen atoms on the quinone ring were used to measure the distances. The methyl groups were classified into the hybridization state of the neighboring covalently bonded atom.

This demonstration is not predictive, and it is difficult to interpret the empirically determined scaling factors of 10 and 50. In this test, the methyl group interactions were all scaled by the same value, but in real systems the importance of a methyl group is likely to depend on its tunneling frequency. We expect that the nature of the atom covalently bound to the methyl group to be the most important predictor of the barrier height, which in turn controls the tunneling frequency,[75] and Fig. 7 collects statistics about the nature of the covalently bound atom for methyl groups near Q_A in bRC and near A_{1A}^- in PSI. We then used density functional theory (M06-2X/cc-pVTZ) to calculate gas phase barrier heights for several residues and cofactors, and we found significant variation in the barrier heights for the different types of methyl groups. Methyl groups bound to O atoms and directly to sp^2 C atoms (as found in the quinones) have low barriers of just 144–370 K, while methyl groups bound to sp^3 C atoms in the amino acids have much larger barrier heights of 1000–1500 K. The larger barrier heights correspond to methyl groups with only a few tunneling events per microsecond, which is roughly the time scale of the coherence dynamics observed here. In contrast, the methyl groups on the quinone with the lower barriers may experience many hundreds or thousands of tunneling events per microsecond. Overall, such a wide range of barrier heights and tunneling event frequencies in the local environment of the electron spin presents a significant challenge to predict numerical modeling of methyl tunneling-induced decay for protein systems.

Conclusions

In this study, we explored the electron spin dynamics of light generated spin-correlated radical pairs in the bRC, focusing on the impact of the local molecular environment and isotopic substitution, particularly deuteration, on electron spin coherence times, T_M. Understanding these dynamics is critical for understanding how quantum spin effects contribute to the function of biological systems, including photosynthetic proteins, as well as for advancing quantum information technologies, where long coherence times are essential for reliable quantum operations.

Our experimental results, obtained through high-frequency EPR spectroscopy, reveal that the microenvironment of the primary donor P_{865} and the quinone acceptor Q_A plays a pivotal role in controlling T_M. Notably, we observed that the coherence times of these spin systems are comparable in both the ''dark'' (stationary) and ''light–dark'' (entangled spin states in SCRP) conditions for protonated bRCs. This indicates that environmental factors, rather than the electron spins entanglement, are significant contributors to spin decoherence.

Deuteration studies provided further insights. While deuteration of only the Q_A acceptor did not significantly extend T_M, full deuteration (protein plus Q_A) led to a modest increase in T_M at low temperatures. However, the anticipated large enhancement in coherence times, typically observed in other systems, was not fully realized in Zn-substituted bRCs. Note that in the case of PSI, full deuteration did not improve electron spin coherence. According to the classical nuclear spin diffusion model, the change in spin coherence times should follow the ratio of nuclear magnetic moments. This is a clear indication that the NSD model alone cannot explain the experimental data in these proteins.

Theoretical modeling corroborated these experimental findings, highlighting the significant impact of methyl group dynamics on spin decoherence, especially at low temperatures. Our simulations showed that the specific structural and dynamic characteristics of the protein environments such as the orientation and proximity of methyl and methylene groups—play a crucial role in determining T_M. Methyl groups, due to their rapid tunneling dynamics, were identified as key contributors to enhanced decoherence in these systems. The theoretical modeling (theoretical mutation), when one or another functional group can be computationally removed or replaced, crucial for this research. This is analog to a very challenging and not always possible experimental approach, when functional groups removed/replaced by biochemical treatment/mutation.

Furthermore, our analysis revealed a strong directional dependence of spin coherence on the orientation of the external magnetic field. The contribution of different chemical groups to decoherence varied with the magnetic field orientation, underscoring the anisotropic influence of the protein structure on spin dynamics. This directional dependence suggests that manipulating the magnetic field relative to the protein structure could optimize spin coherence times, an important consideration for designing quantum devices.

This study expands our knowledge on the mechanisms underlying spin decoherence in photosynthetic RCs and emphasizes the critical role of the local molecular environment, particularly the dynamics of methyl groups, in modulating T_M. These insights are fundamental for the development of protein-based quantum devices and suggest new strategies for optimizing coherence times in quantum systems. Future research will focus on refining theoretical models to include more accurate descriptions of methyl tunneling effects and further exploring the potential of these proteins as stable qubits in quantum technologies. This work represents a significant advancement in leveraging biological systems for quantum information science.

Abbreviations

QIS	Quantum information science
mw/rf	Microwave/radio frequency
RC	Reaction center
ET	Electron transfer
PSI	Photosystem I
SCRPs	Spin correlated radical pairs
SQP	Spin qubit pair
NSD	Nuclear spin diffusion
EPR	Electron paramagnetic resonance
ESE	Electron spin echo

DAF	Delay after laser flash
ESEEM	Electron spin echo modulation
HFI	Hyperfine interaction

Author information

Jasleen K. Bindra and Yeonjun Jeong: investigation, methodology, writing – original draft, visualization, Jens Niklas, Ahren W. Jasper, Lisa M. Utschig, and Oleg G. Poluektov: supervision, conceptualization, resources, writing – review & editing.

Data availability

The data supporting this article have been included as part of the ESI.†

Conflicts of interest

There are no conflicts to declare.

Acknowledgements

This material is based upon work supported by the U.S. Department of Energy, Office of Science, Office of Basic Energy Sciences, Division of Chemical Sciences, Geosciences, and Biosciences, under contract number DE-AC02-06CH11357 at Argonne National Laboratory. We gratefully acknowledge use of the high-performance computing resources operated by the Laboratory Computing Resource Center at Argonne National Laboratory.

Notes and references

1 M. R. Wasielewski, M. D. E. Forbes, N. L. Frank, K. Kowalski, G. D. Scholes, J. Yuen-Zhou, M. A. Baldo, D. E. Freedman, R. H. Goldsmith, T. Goodson, M. L. Kirk, J. K. McCusker, J. P. Ogilvie, D. A. Shultz, S. Stoll and K. B. Whaley, *Nat. Rev. Chem.*, 2020, **4**, 490–504.
2 J. M. Zadrozny, J. Niklas, O. G. Poluektov and D. E. Freedman, *J. Am. Chem. Soc.*, 2014, **136**, 15841–15844.
3 H. J. Mamin, M. Kim, M. H. Sherwood, C. T. Rettner, K. Ohno, D. D. Awschalom and D. Rugar, *Science*, 2013, **339**, 557–560.
4 P. C. Maurer, G. Kucsko, C. Latta, L. Jiang, N. Y. Yao, S. D. Bennett, F. Pastawski, D. Hunger, N. Chisholm, M. Markham, D. J. Twitchen, J. I. Cirac and M. D. Lukin, *Science*, 2012, **336**, 1283–1286.
5 S. L. Bayliss, D. W. Laorenza, P. J. Mintun, B. D. Kovos, D. E. Freedman and D. D. Awschalom, *Science*, 2020, **370**, 1309–1312.
6 C. J. Yu, M. J. Graham, J. M. Zadrozny, J. Niklas, M. D. Krzyaniak, M. R. Wasielewski, O. G. Poluektov and D. E. Freedman, *J. Am. Chem. Soc.*, 2016, **138**, 14678–14685.
7 J. M. Zadrozny, J. Niklas, O. G. Poluektov and D. E. Freedman, *ACS Cent. Sci.*, 2015, **1**, 488–492.
8 S. M. Harvey and M. R. Wasielewski, *J. Am. Chem. Soc.*, 2021, **143**, 15508–15529.
9 T. Mani, *Chem. Phys. Rev.*, 2022, **3**, 021301.
10 O. G. Poluektov, J. Niklas and L. M. Utschig, *J. Phys. Chem. B*, 2019, **123**, 7536–7544.
11 R. Bittl and S. Weber, *Biochim. Biophys. Acta*, 2005, **1707**, 117–126.
12 A. van der Est, T. Prisner, R. Bittl, P. Fromme, W. Lubitz, K. Mobius and D. Stehlik, *J. Phys. Chem. B*, 1997, **101**, 1437–1443.
13 O. G. Poluektov, S. V. Paschenko, L. M. Utschig, K. V. Lakshmi and M. C. Thurnauer, *J. Am. Chem. Soc.*, 2005, **127**, 11910–11911.
14 R. Bittl and S. G. Zech, *Biochim. Biophys. Acta*, 2001, **1507**, 194–211.
15 S. Santabarbara, I. Kuprov, W. V. Fairclough, S. Purton, P. J. Hore, P. Heathcote and M. C. W. Evans, *Biochemistry*, 2005, **44**, 2119–2128.
16 T. Berthold, E. D. von Gromoff, S. Santabarbara, P. Stehle, G. Link, O. G. Poluektov, P. Heathcote, C. F. Beck, M. C. Thurnauer and G. Kothe, *J. Am. Chem. Soc.*, 2012, **134**, 5563–5576.
17 S. Santabarbara, K. Reifschneider, A. Jasaitis, F. F. Gu, G. Agostini, D. Carbonera, F. Rappaport and K. E. Redding, *J. Phys. Chem. B*, 2010, **114**, 9300–9312.
18 J. Niklas, B. Epel, M. L. Antonkine, S. Sinnecker, M. E. Pandelia and W. Lubitz, *J. Phys. Chem. B*, 2009, **113**, 10367–10379.
19 A. Savitsky, J. Niklas, J. H. Golbeck, K. Mobius and W. Lubitz, *J. Phys. Chem. B*, 2013, **117**, 11184–11199.
20 O. G. Poluektov and L. M. Utschig, *J. Phys. Chem. B*, 2021, **125**, 4025–4030.
21 S. G. Zech, W. Hofbauer, A. Kamlowski, P. Fromme, D. Stehlik, W. Lubitz and R. Bittl, *J. Phys. Chem. B*, 2000, **104**, 9728–9739.
22 O. G. Poluektov, S. V. Paschenko and L. M. Utschig, *Phys. Chem. Chem. Phys.*, 2009, **11**, 6750–6756.
23 B. Epel, J. Niklas, M. L. Antonkine and W. Lubitz, *Appl. Magn. Reson.*, 2006, **30**, 311–327.
24 Y. H. Huang, Y. F. Qiu, R. M. Young, G. C. Schatz, M. D. Krzyaniak and M. R. Wasielewski, *J. Am. Chem. Soc.*, 2024, **146**, 20133–20140.
25 L. Bancroft, Y. F. Qiu, M. D. Krzyaniak and M. R. Wasielewski, *J. Phys. Chem. Lett.*, 2022, **13**, 156–160.
26 B. K. Rugg, M. D. Krzyaniak, B. T. Phelan, M. A. Ratner, R. M. Young and M. R. Wasielewski, *Nat. Chem.*, 2019, **11**, 981–986.
27 P. J. Hore and H. Mouritsen, *Annu. Rev. Biophys.*, 2016, **45**, 299–344.
28 R. Wiltschko and W. Wiltschko, *J. R. Soc., Interface*, 2019, **16**, 20190295.
29 J. Tang, L. M. Utschig, O. Poluektov and M. C. Thurnauer, *J. Phys. Chem. B*, 1999, **103**, 5145–5150.
30 T. F. Prisner, A. Vanderest, R. Bittl, W. Lubitz, D. Stehlik and K. Mobius, *Chem. Phys.*, 1995, **194**, 361–370.
31 S. A. Dzuba, P. Gast and A. J. Hoff, *Chem. Phys. Lett.*, 1995, **236**, 595–602.

32 R. E. Blankenship, *Molecular Mechanisms of Photosynthesis*, Blackwell Science Limited, Oxford, UK, 2002.
33 O. G. Poluektov and L. M. Utschig, *J. Phys. Chem. B*, 2015, **119**, 13771–13776.
34 J. P. Allen, G. Feher, T. O. Yeates, H. Komiya and D. C. Rees, *Proc. Natl. Acad. Sci. U. S. A.*, 1988, **85**, 8487–8491.
35 C. H. Chang, O. Elkabbani, D. Tiede, J. Norris and M. Schiffer, *Biochemistry*, 1991, **30**, 5352–5360.
36 U. Ermler, G. Fritzsch, S. K. Buchanan and H. Michel, *Structure*, 1994, **2**, 925–936.
37 A. J. Hoff and J. Deisenhofer, *Phys. Rep.*, 1997, **287**, 1–247.
38 G. Feher, J. P. Allen, M. Y. Okamura and D. C. Rees, *Nature*, 1989, **339**, 111–116.
39 L. M. G. Utschig, S. R. Greenfield, J. Tang, P. D. Laible and M. C. Thurnauer, *Biochemistry*, 1997, **36**, 8548–8558.
40 J. K. Bindra, J. Niklas, Y. Jeong, A. W. Jasper, M. Kretzschmar, J. Kern, L. M. Utschig and O. G. Poluektov, *J. Phys. Chem. B*, 2023, **127**, 10108–10117.
41 Y. Jeong, J. K. Bindra, J. Niklas, L. M. Utschig, O. G. Poluektov and A. W. Jasper, *Appl. Phys. Lett.*, 2024, **124**, 044001.
42 G. Jeschke, *Appl. Magn. Reson.*, 2022, **53**, 635–651.
43 W. Yang and R. B. Liu, *Phys. Rev. B: Condens. Matter Mater. Phys.*, 2008, **78**, 085315.
44 A. J. Horsewill, *Prog. Nucl. Magn. Reson. Spectrosc.*, 1999, **35**, 359–389.
45 M. Simenas, D. Klose, M. Ptak, K. Aidas, M. Maczka, J. Banys, A. Pöppl and G. Jeschke, *Sci. Adv.*, 2020, **6**, eaba1517.
46 J. Soetbeer, L. F. Ibáñez, Z. Berkson, Y. Polyhach and G. Jeschke, *Phys. Chem. Chem. Phys.*, 2021, **23**, 21664–21676.
47 A. Eggeling, J. Soetbeer, L. Fábregas-Ibáñez, D. Klose and G. Jeschke, *Phys. Chem. Chem. Phys.*, 2023, **25**, 11145–11157.
48 R. Erickson, U. Nordh, N. P. Benetis and A. Lund, *Chem. Phys.*, 1992, **168**, 91–98.
49 R. J. Debus, G. Feher and M. Y. Okamura, *Biochemistry*, 1986, **25**, 2276–2287.
50 L. M. Utschig, M. C. Thurnauer, D. M. Tiede and O. G. Poluektov, *Biochemistry*, 2005, **44**, 14131–14142.
51 A. Y. Bresgunov, A. A. Dubinskii, V. N. Krimov, Y. G. Petrov, O. G. Poluektov and Y. S. Lebedev, *Appl. Magn. Reson.*, 1991, **2**, 715–728.
52 O. G. Poluektov, L. M. Utschig, S. L. Schlesselman, K. V. Lakshmi, G. W. Brudvig, G. Kothe and M. C. Thurnauer, *J. Phys. Chem. B*, 2002, **106**, 8911–8916.
53 G. Kothe and M. C. Thurnauer, *Photosynth. Res.*, 2009, **102**, 349–365.
54 R. Bittl and G. Kothe, *Chem. Phys. Lett.*, 1991, **177**, 547–553.
55 O. G. Poluektov, L. M. Utschig, A. A. Dubinskij and M. C. Thurnauer, *J. Am. Chem. Soc.*, 2005, **127**, 4049–4059.
56 A. Savitsky, A. A. Dubinskii, M. Flores, W. Lubitz and K. Möbius, *J. Phys. Chem. B*, 2007, **111**, 6245–6262.
57 J. K. Bindra, T. Malavath, M. Y. Teferi, M. Kretzschmar, J. Kern, J. Niklas, L. M. Utschig and O. G. Poluektov, *Int. J. Mol. Sci.*, 2024, **25**, 8188.
58 J. K. Bindra, J. Niklas, Y. Jeong, A. W. Jasper, M. Kretzschmar, J. Kern, L. M. Utschig and O. G. Poluektov, *J. Phys. Chem. B*, 2023, **127**, 10108–10117.
59 J. Tang, M. C. Thurnauer and J. R. Norris, *Chem. Phys. Lett.*, 1994, **219**, 283–290.
60 A. J. Schweiger and G. Jeschke, *Principles of Pulse Electron-Paramagnetic Resonance*, Oxford University Press, 2001.
61 G. Jeschke, *J. Magn. Reson. Open*, 2023, **14**, 100094.
62 S. S. Eaton and G. R. Eaton, *Relaxation times of organic radicals and transition metal ions*, Springer, Boston, 2000, pp. 29–154.
63 S. M. Jahn, E. R. Canarie and S. Stoll, *J. Phys. Chem. Lett.*, 2022, 5474–5479.
64 I. M. Brown, Electron Spin-Echo Studies of RelaxationProcesses in Molecular Solids, *Time Domain Electron SpinResonance*, Wiley, New York, 1979.
65 J. You, D. Carić, B. Rakvin, Z. Stefanic, K. Uzarevic and M. Kveder, *J. Chem. Phys.*, 2019, **150**, 164124.
66 M. Onizhuk and G. L. Galli, *Adv. Theor. Simul.*, 2021, **4**, 2100254.
67 J. Koepke, E. M. Krammer, A. R. Klingen, P. Sebban, G. M. Ullmann and G. Fritzsch, *J. Mol. Biol.*, 2007, **371**, 396–409.
68 N. M. O'Boyle, M. Banck, C. A. James, C. Morley, T. Vandermeersch and G. R. Hutchison, *J. Cheminf.*, 2011, **3**, 33.
69 M. Lindgren, G. R. Eaton, S. S. Eaton, B. H. Jonsson, P. Hammarstrom, M. Svensson and U. Carlsson, *J. Chem. Soc., Perkin Trans. 2*, 1997, 2549–2554.
70 L. J. Berliner, G. R. Eaton and S. S. Eaton, *Distance Measurements in Biological Systems by EPR*, Springer, Boston, 2000.
71 M. Huber, M. Lindgren, P. Hammarström, L. G. Mårtensson, U. Carlsson, G. R. Eaton and S. S. Eaton, *Biophys. Chem.*, 2001, **94**, 245–256.
72 E. R. Canarie, S. M. Jahn and S. Stoll, *J. Phys. Chem. Lett.*, 2020, **11**, 3396–3400.
73 J. F. Du, X. Rong, N. Zhao, Y. Wang, J. H. Yang and R. B. Liu, *Nature*, 2009, **461**, 1265–1268.
74 M. Kveder, B. Rakvin and J. Y. You, *J. Chem. Phys.*, 2019, **151**, 164124.
75 R. M. Dimeo, *Am. J. Phys.*, 2003, **71**, 885–893.